Christian Ziese
Institute of Mechanics,
Otto von Guericke University,
Magdeburg 39106, Germany
e-mail: christian.ziese@ovgu.de

Cornelius Irmscher
Institute of Mechanics,
Otto von Guericke University,
Magdeburg 39106, Germany
e-mail: cornelius.irmscher@ovgu.de

Steffen Nitzschke
Institute of Mechanics,
Otto von Guericke University,
Magdeburg 39106, Germany
e-mail: steffen.nitzschke@ovgu.de

Christian Daniel
Institute of Mechanics,
Otto von Guericke University,
Magdeburg 39106, Germany
e-mail: christian.daniel@ovgu.de

Elmar Woschke
Institute of Mechanics,
Otto von Guericke University,
Magdeburg 39106, Germany
e-mail: elmar.woschke@ovgu.de

Thomas Klimpel
ABB Turbocharging,
Baden 5401, Switzerland
e-mail: Thomas.Klimpel@ch.abb.com

Influence of Lubricant Film Cavitation on the Vibration Behavior of a Semifloating Ring Supported Turbocharger Rotor With Thrust Bearing

This contribution investigates the influence of outgassing processes on the vibration behavior of a hydrodynamic bearing supported turbocharger rotor. The examined rotor is supported radially by floating rings with outer squeeze-film damping and axially by thrust bearings. Due to the highly nonlinear bearing properties, the rotor can be excited via the lubricating film, which results in subsynchronous vibrations known as oil-whirl and oil-whip phenomena. A significant influence on the occurrence of oil-whip phenomena is attributed to the bearing stiffness and damping, which depend on the kinematic state of the supporting elements, the thermal condition, and the occurrence of outgassing processes. For modeling the bearing behavior, the Reynolds equation with mass-conserving cavitation regarding the two-phase model and the three-dimensional (3D) energy as well as heat conduction equation is solved. To evaluate the impact of cavitation, run-up simulations are carried out assuming a fully (half-Sommerfeld) or partially filled lubrication gap. The resulting rotor responses are compared with the shaft motion measurement. Also, the normalized eccentricity, the minimum lubricant fraction, and the thermal bearing condition are discussed. [DOI: 10.1115/1.4053266]

1 Introduction

The support of fast rotating rotors is usually realized via hydrodynamic bearings, since they have a simple and cost-efficient design and more favorable thermohydrodynamic conditions. However, this bearing type exhibits a highly nonlinear behavior, leading to lubricant film-induced rotor excitations in terms of subsynchronous vibrations. To be more specific, the excitation mechanism takes place via the half-whirl frequency of the oil (oil-whirl) in the lubrication gap of the journal bearing [1]. If the oil-whirl coincides with a current and weakly damped rotor's natural frequency, increased vibration amplitudes can occur, leading to additional wear and even rotor failure. For these reasons, detailed modeling of the bearing behavior is necessary to enable reliable prediction of rotor vibrations.

The occurrence of subsynchronous vibrations depends on numerous factors. In addition to the rotor's mass distribution and stiffness, the stiffness and damping properties of the individual bearings as well as their arrangement and acting loads are essential [2–5]. Outgassing processes have significant influences on the bearing properties, since a multiphase flow consisting of the oil and gas can occur in the lubrication gap. In Ref. [6], a distinction is made between vapor and gas cavitation and the penetration of air from the environment (aeration). Vapor cavitation occurs if the hydrodynamic pressure falls below the vapor pressure, so the lubricant changes its aggregate state. In contrast, gas cavitation is

a diffusion-induced process. If the pressure falls below the saturation pressure, the gas dissolved in the lubricant undergoes a phase transition and is present as a separate phase in the lubrication gap. The occurrence of outgassing processes influences the pressure distribution and thus the bearing stiffness and damping. Regarding the bearing conditions of the investigated rotor, diffusion processes are assumed in the lubrication gap. Vapor cavitation can lead to surface damages since the bubbles collapse abruptly; aeration causes insufficient lubrication of the gap. Neither effect occurred during the operation of the turbocharger. If outgassing processes appear in journal bearings for turbocharger rotors, it is mainly gas cavitation.

Experimental investigations concerning the influence of gas-phase on the pressure distribution and resulting forces at journal bearings can be found in Refs. [6–11] and for thrust bearing in Refs. [12–14]. In Ref. [11], various manifestations of the cavitation domain are observed at squeeze-film damper. Depending on the operating bearing condition, the surface roughnesses on the shaft and housing, as well as the degree of purity of the oil, mostly larger fern leaf-shaped or numerous smaller bubbles appear. Andres and Lu [10] investigate the influence of the separate gas-phase on the bearing stiffness and damping. Therein, the gas volume fraction in the lubrication gap is varied by an external gas supply, and the resulting oscillation responses are measured. In summary, the bearing reacts softer with increasing gas volume fraction, so even subsynchronous oscillations of the seal cartridge can be observed. In addition to the already mentioned impact factors, the surface texture should also be mentioned for completeness. This is examined more in detail by Bai et al. [14] for thrust bearings.

For modeling of outgassing processes, the theory of Jakobsson, Floberg, and Olsson and, based on this, the cavitation algorithm according to Elrod [15–18], the bubble dynamics with the Rayleigh–Plesset equation [19–23], and the two-phase model [24–27] are known as mass-conserving cavitation models. Concerning the Elrod algorithm, constant pressure is assumed in the cavitation domain. Furthermore, a switch function is introduced to distinguish between the pressure and cavitation domain, which depends on the hydrodynamic pressure and lubricant fraction (summarized as a universal variable). Nitzschke et al. [16] implemented the Elrod algorithm with a continuous transition (regularization) between the pressure and cavitation state. This approach enables the application of the Newton–Raphson method for efficient implementation. However, the negligence of temperature influences is a disadvantage. The Rayleigh–Plesset equation is derived from the Navier–Stokes equation. It is a second-order differential equation that describes the growth of the bubbles as a function of the hydrodynamic pressure, bubble inertia, and surface tensions [21,22]. In the sense of efficient implementation for transient rotor dynamic analysis, the Rayleigh–Plesset equation is not recommended, since, besides the Reynolds equation, a further equation has to be solved within the time integration. Finally, in terms of efficient implementation and the consideration of temperature influences, the two-phase model is preferred in this contribution. Gas cavitation is modeled by balancing the gas masses dissolved in the lubricant and the separate gas-phase. As a consequence, there is a direct correlation between the lubricant fraction and the hydrodynamic pressure as well as the oil film temperature.

The influence of outgassing processes on the rotor vibration behavior is investigated in Refs. [28–30]. However, the examination refers to full-floating ring supported Jeffcott rotors and turbocharger rotors for passenger car engines. There, the rotor can be excited via the inner and outer lubricant film. Ziese et al. [26] examined a semifloating ring supported turbocharger rotor under the influence of the thrust bearing. As a result, the rotor's oscillation mode can be influenced by taking the tilting stiffness of the thrust bearing into account. Furthermore, the current natural frequency of the rotor can be shifted closer to the half-whirl frequency of the journal bearing so that an oil-whip is created. Further investigations of turbocharger vibrations with semifloating bearings can be found in Refs. [31–33]. In contrast to full-floating ring bearings, rotor excitation only occurs through the inner lubrication gap of the journal bearing. The outer gap contributes to the bearing damping.

In the context of nonlinear rotor vibrations, investigations can be found in Refs. [34–44]. Schweizer [34] examed the stability of a full-floating ring supported turbocharger rotor. It was found that when the inner oil film becomes unstable (oil-whip in the inner lubricating film), the outer oil film has dampening effects on the vibration behavior of the rotor due to the oil film squeezing. It is also possible that the outer lubricating film excites the rotor, and the inner one has damping effects. Nowald et al. [40] investigated the rotor vibration behavior depending on the axial grooves in the bushing. Run-up results with axial grooves were compared with simulations using unprofiled plain bearings. It was found that axial grooves can reduce the amplitude of the subsynchronous oscillations, but the third oil-whip is shifted to lower frequencies. In Ref. [41], the rotor response was evaluated considering thrust bearings. The Reynolds equation is solved for the hydrodynamics, and the three-dimensional (3D) energy equation is used for modeling thermal processes in thrust bearings. However, the short bearing theory is applied for journal bearings. The influence of various cavitation theories on the rotor response was investigated by Dong et al. [44]. For completeness, it should be mentioned that the nonlinear vibration behavior can also be evaluated via bifurcation. Bifurcation investigations were carried out by Boyaci et al. [45–47] and Becker [48].

Based on the rotor examined by Ziese et al. [26], this contribution focuses on the effects of outgassing processes on the rotor vibration behavior. In Ref. [26], a comparison of the run-up behavior with and without thrust bearing was made. This includes the shaft and bushing motion depending on the tilting stiffness of the thrust bearing. In this contribution, the investigation focuses on the influence of cavitation. For this purpose, a comparison of the rotor response is made under the assumption of a fully (half-Sommerfeld) or partially (two-phase model) filled lubrication gap. The influence of cavitation is shown by the rotor vibrations in the time and frequency domain, the supporting elements' motion orbit, and the lubricant fraction in the bearings. Furthermore, the thermal bearing state is discussed more in detail. Concerning the modeling of the hydrodynamics at journal and thrust bearings, the Reynolds equation with mass-conserving cavitation according to the two-phase model is used. In floating ring bearings, thermal influences are taken into account using the 3D energy equation to determine the temperature distribution in the oil film and the heat conduction equation for shaft, bushing, and housing.

2 Rotor Bearing Model

Subject of investigation is a semifloating ring with outer squeeze-film damping supported turbocharger rotor consisting of a radial compressor and turbine wheel, sealing disk, thrust ring, and auxiliary bearing, see Fig. 1. Due to the mass distribution, the overall center of gravity is close to the turbine bearing, which has the consequence that the rotor generally tends to tilt. For this reason, the consideration of the thrust bearing is necessary for a precise prediction of the rotor oscillations. The total rotor mass and length is $m_{\mathrm{Rot}} = 20$ kg and $l_{\mathrm{Rot}} = 0.450$ m. The unbalance distribution is known with u_C and u_T by measurements. To model the rotor deformation, the finite element method is applied according to the Timoshenko beam theory. The FE nodes are located at shaft shoulders as well as at journal and thrust bearings in order to determine the lubrication gap. In addition to the rotor, the floating rings have to be considered as separate bodies within the multibody simulation. The interactions between the individual bodies take place via resulting forces and torques due to the hydrodynamic pressure distribution. Consequently, forces act between shaft and bushing (inner oil film) and between bushing and housing (outer oil film). With regard to the thrust bearing, the forces and torques act between the housing and the auxiliary bearing or thrust ring.

Besides the rotor model, the bearing design is described. With regard to the floating ring bearings, the inner lubrication gap has a multilobe surface consisting of three segments. The outer gap has a circumferential groove to ensure sufficient lubricant supply. For the bearings considered here, the lubricant can flow out freely over the edge (nonsealed bearing), cf. Fig. 2. Concerning the degrees-of-freedom of the bushing within the multibody simulation, the ring can move horizontally (x_I-direction) and vertically (y_I-direction), but tilting is neglected. Thus, there is a parallel gap at the outer oil film. However, the shaft tilting is taken into account at the inner gap.
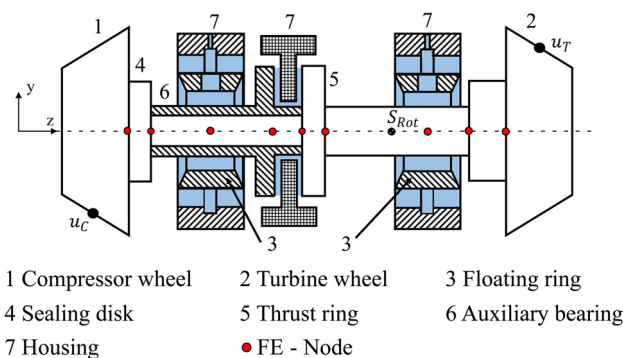

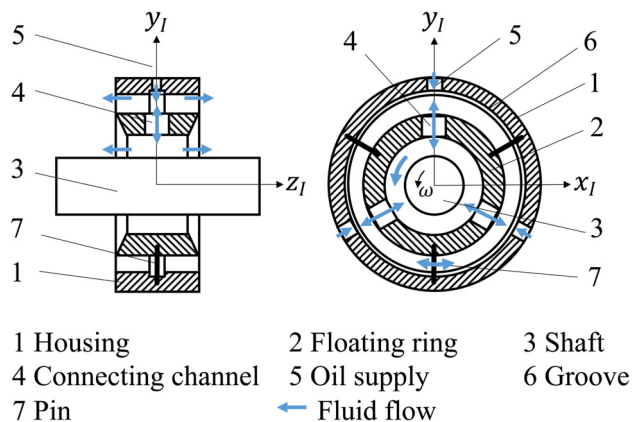**Fig. 1 Schematic design of rotor model [26]**

1 Compressor wheel	2 Turbine wheel	3 Floating ring
4 Sealing disk	5 Thrust ring	6 Auxiliary bearing
7 Housing	● FE - Node	

1 Housing 2 Floating ring 3 Shaft
4 Connecting channel 5 Oil supply 6 Groove
7 Pin ← Fluid flow

Fig. 2 Schematic design of a semifloating ring bearing [26]. The inertial system for the multibody simulation is x_I, y_I, z_I, where the z_I axis is equal to the longitudinal rotor axis.

The axial support of the rotor is realized via two thrust bearings, see Fig. 3. The compressor- and turbine-sided axial gap consists of eight segments, whereby each of them has a wedge, flat, and groove area. Furthermore, the bearing is sealed at the outer edge. The sealing effect is achieved because the outer edge has no contour. Due to the oil supply and the arrangement of the bearings, both thrust bearings are considered separately from each other, and thermal coupling is neglected for simplicity. Regarding the degrees-of-freedom within the multibody simulation, the rotor can move freely (no degrees-of-freedom are locked).

In Secs. 2.1–2.4, the theoretical fundamentals for determining the pressure distribution in hydrodynamic bearings are discussed. This includes the evaluation of the Reynolds equation with mass-conserving cavitation according to the two-phase model. Furthermore, the modeling of the thermodynamic processes in the lubricating film and at supporting elements as well as their coupling to each other is described.

2.1 Reynolds Equation. To determine the pressure distribution for a laminar and incompressible flow in hydrodynamic bearings, the Reynolds equation

$$0 = -\frac{\partial}{\partial x}\left(\frac{\rho h^3}{12\eta}\frac{\partial p}{\partial x}\right) - \frac{\partial}{\partial y}\left(\frac{\rho h^3}{12\eta}\frac{\partial p}{\partial y}\right) + \frac{\partial}{\partial x}\left(\rho h \frac{u_S + u_H}{2}\right) + \frac{\partial}{\partial t}(\rho h) \qquad (1)$$
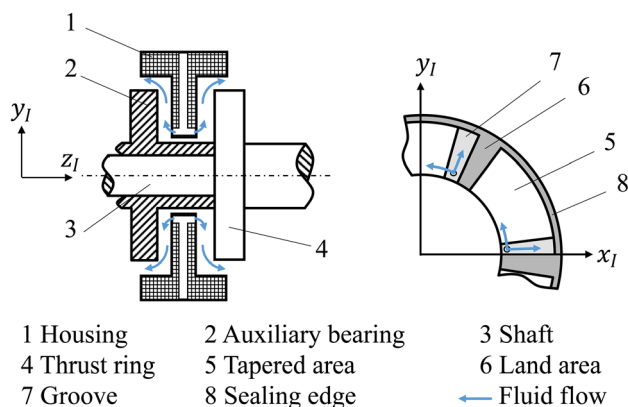

1 Housing 2 Auxiliary bearing 3 Shaft
4 Thrust ring 5 Tapered area 6 Land area
7 Groove 8 Sealing edge ← Fluid flow

Fig. 3 Schematic design of a thrust bearing [26]. The x_I, y_I, z_I coordinate system represents the inertial system of the multibody simulation.

for journal bearings and

$$0 = -\frac{\partial}{r\partial r}\left(r\frac{\rho h^3}{12\eta}\frac{\partial p}{\partial r}\right) - \frac{\partial}{r\partial \varphi}\left(\frac{\rho h^3}{12\eta}\frac{\partial p}{r\partial \varphi}\right) + \frac{\partial}{r\partial \varphi}\left(\rho h \frac{u_{\varphi S} + u_{\varphi H}}{2}\right) + \frac{\partial}{\partial t}(\rho h) + \frac{\partial}{r\partial r}\left(\frac{\rho^2 h^3}{\eta}\left(\frac{u_{\varphi S}^2}{40} + \frac{u_{\varphi S} u_{\varphi H}}{30} + \frac{u_{\varphi H}^2}{40}\right)\right) \qquad (2)$$

for thrust bearings are evaluated. Therein, p is the hydrodynamic pressure, ρ is the density and η is viscosity of the oil, h is the gap height, and t is the time. For journal bearings, a Cartesian coordinate system is used for the lubrication gap, where x is the circumferential and y is the width coordinate. In contrast, the pressure distribution in thrust bearings is described in a cylindrical coordinate system. Since an ideal adhesion between the surface of shaft/disk or housing and the fluid is assumed, the kinematic states of the supporting elements can be used as boundary conditions of the fluid flow. Consequently, the circumferential velocities for the shaft and housing u_S and u_H at journal bearing as well as $u_{\varphi S}$ and $u_{\varphi H}$ at thrust bearing are known.

Concerning the thrust bearings, the influence of the fluid inertia has to be taken into account, since this causes an additional flow in radial direction. The centrifugal flow is determined by the circumferential velocity of the fluid, which is composed of the shear-induced and pressure-induced flow. However, in this contribution, the centrifugal flow is mainly generated by the shear components (Couette flow) and less by the pressure gradient (Poiseuille-flow) due to the kinematic states of the supporting elements. Furthermore, the coefficients of the pressure-induced inertia component have powers of the gap height of fifth and seventh order. Compared to the coefficient of shear flow (lubrication gap power of third-order), these can be neglected. An extension of the centrifugal flow concerning the pressure-induced influence can be found in Refs. [13,49], and [50].

For the sake of completeness, it should be mentioned that fluid inertia effects can also occur in journal bearing. These are neglected in this contribution, since the modified Reynolds number of the bearings is Re* < 1. The modified Reynolds number is calculated via

$$\text{Re}^\star = \frac{\rho \omega c^2}{\eta} \qquad (3)$$

where c is the absolute bearing clearance, and ω is the circumferential excitation frequency. The Reynolds equation with fluid inertia effects in journal bearings is documented in Refs. [51] and [52].

Furthermore, the generalized Reynolds equation can also be used to describe the hydrodynamics in bearings. But due to the operating boundary conditions of the investigated turbocharger (high oil inlet temperature), the thermal change of viscosity is low, so the integral terms of the generalized Reynolds equation can be simplified. Another reason for using Eqs. (1) and (2) instead of the generalized Reynolds equation is the significantly lower computing times, since the integral terms do not have to be determined additionally. The run-up simulations with generalized Reynolds equation show similar results, see Appendix in Ref. [26].

For floating ring bearings, the lubricant exchange between the inner and outer gap must be taken into account. Depending on the operating bearing condition, the oil can flow from the inner to the outer gap or vice versa. To model the fluid flow in the connecting channel, a cylindrical coordinate system according to Fig. 4 is used, and a simplified representation of the Navier–Stokes equation

$$\frac{1}{r}\frac{\partial}{\partial r}\left(r\eta\frac{\partial u_z}{\partial r}\right) = C = \frac{\partial p}{\partial z} \qquad (4)$$
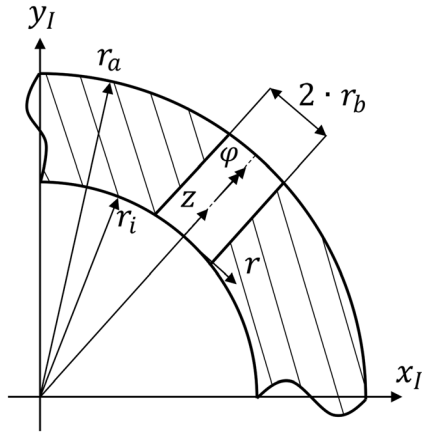
Fig. 4 Coordinate system for coupling the lubricating films in floating ring bearings, according to Nitzschke [18]

is evaluated [18,53]. For solving Eq. (4), it is assumed that there is an axially symmetric $(\partial/\partial\varphi = 0)$, stationary $(\partial/\partial z = 0)$, and fully developed $(\partial/\partial z = 0)$ pipe flow.

The solution of Eq. (4) provides the velocity profile [53]

$$u_z(r) = \frac{r^2 - r_b^2}{4\eta(r_a - r_i)}[p_a - p_i] \tag{5}$$

and the mass flow in the channel

$$\dot{m} = \int_{\varphi=0}^{2\pi} \int_{r=0}^{r_b} \rho\, u_z\, r dr d\varphi$$
$$= \frac{\pi r_b^4}{8(r_a - r_i)} \frac{\rho}{\eta}[p_a - p_i] \tag{6}$$

There, p_i is the pressure from the inner and p_a from the outer lubrication gap. Lubricant exchange takes place if there is a pressure gradient in the channel. For numerical implementation, the mass flow in the connecting channel is added to the Reynolds equation for the inner and outer oil film. The equations of hydrodynamics are solved as a fully coupled system.

2.2 Two-Phase Flow Model. As mentioned in the Introduction, a two-phase flow occurs in the lubrication gap in case of outgassing processes. For modeling of gas cavitation, the two-phase model is implemented, in which the gas masses dissolved in the oil and present separately are balanced. The aim is to determine a correlation between the lubricant fraction, the hydrodynamic pressure, and oil temperature. For this purpose, a partially filled lubrication gap is considered, whereby the phase transition takes place via the bubble surface, see Fig. 5.
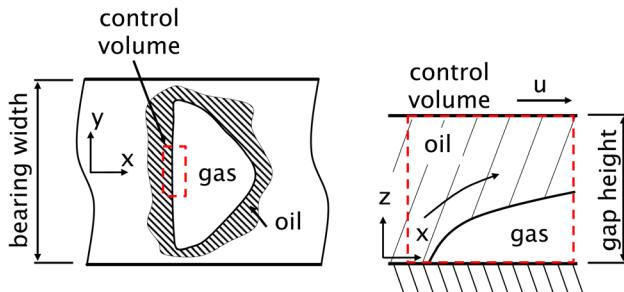

Fig. 5 Partially filled lubrication gap [54]

Regarding the Reynolds equations (1) and (2), respectively, it becomes clear that the hydrodynamic pressure and thus also the resulting bearing forces depend on the oil properties. In contrast, the properties of the separate gas-phase and the gas molecularly dissolved in the lubricant can be neglected for further calculations. To take the influence of the lubricant fraction on the pressure distribution into account, effective lubricant properties according to

$$\eta_{\text{eff}} = \eta_{\text{liq}}F + \eta_g(1 - F) \approx \eta_{\text{liq}}F$$
$$\rho_{\text{eff}} = \rho_{\text{liq}}F + \rho_g(1 - F) \approx \rho_{\text{liq}}F \tag{7}$$

are introduced. The lubricant fraction F represents the ratio of the lubricant volume V_{liq} (hatched area) to the size of the control volume V_{CV} (red dashed area). The bubble content r_B is determined via the ratio of the gas (white area) and oil volume

$$F = \frac{V_{\text{oil}}}{V_{\text{CV}}} = \frac{1}{1 + r_B} \tag{8}$$

$$r_B = \frac{V_B}{V_{\text{oil}}} \tag{9}$$

Basis for the two-phase model is the determination of the lubricant-dissolved m_{Bdis} and separate m_{Bundis} gas masses. The total mass of gas m_B remains constant during the outgassing process, but the individual parts can undergo a phase transition

$$m_B = m_{Bdis} + m_{Bundis} = \text{const.} \tag{10}$$

To determine the undissolved gas mass, the ideal gas law

$$m_{Bundis} = V_B \frac{p}{RT} \tag{11}$$

is used, where p denotes the hydrodynamic pressure, R denotes the specific gas constant, and T denotes the absolute temperature of the lubricant. The gas masses dissolved in the oil are calculated via the ideal gas law with application of the Bunsen solubility (Henry's law)

$$V_{Bdis} = \alpha_B V_{\text{oil}} \frac{p}{p_0} \tag{12}$$

$$m_{Bdis} = V_{Bdis} \frac{p}{RT} = \alpha_B V_{\text{oil}} \frac{p^2}{p_0 RT} \tag{13}$$

The Bunsen solubility describes the solubility of gases in liquids and can be used for the idealized modeling of the time-dependent diffusion process between dissolved and undissolved gas masses. According to Eq. (12), the dissolved gas volume is linearly dependent on the pressure and the available oil volume. The Bunsen coefficient α_B depends on the oil and the chemical composition of the gas, but can be assumed to be constant $\alpha_B \approx 0.08 - 0.09$ for the mineral oils ISO-VG 32-220 [55,56].

Inserting Eqs. (11) and (13) into Eq. (10) with the definition of the bubble content Eq. (9) yields the total mass of gas

$$m_B = \left(r_B + \alpha_B \frac{p}{p_0}\right) \frac{V_{\text{oil}}\, p}{R\, T} = \text{const.} \tag{14}$$

The assumption of a constant total mass of gas offers the possibility to compare the current operating bearing condition with a reference one, cf. Fig. 6. With regard to the reference state, the hydrodynamic pressure p_0, the lubricant temperature T_0, and the already undissolved gas masses with the reference bubble content r_{B0} are known, so the total gas mass can be determined via Eq. (14).

Besides the reference state, the current bearing state must be considered. An increasing hydrodynamic pressure leads to a phase
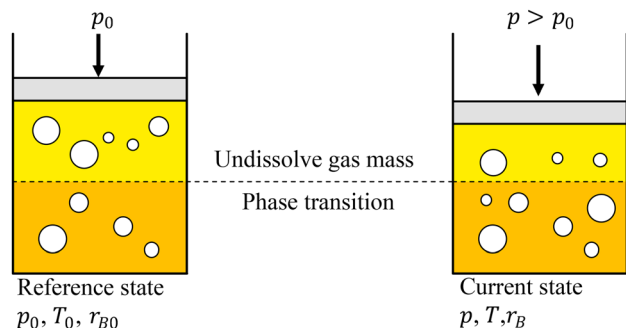
Fig. 6 Comparison of current operating bearing condition with reference state, according to Mermertas [56]

transition of the gas masses from undissolved to dissolved state at constant temperature. As a result, the amount of separately existing gas masses decreases and the lubricant fraction increases. Similarly, a decrease in hydrodynamic pressure leads to a phase transition from the dissolved to the undissolved gas state. Consequently, outgassing processes take place.

In addition to the hydrodynamic pressure, the influence of the lubricant film temperature on the gas generation is also given, see Fig. 7. A cavitation domain is present if the lubricant fraction $F \leq 1$, otherwise it is a pressure domain with a completely filled gap. The influence of the oil temperature is shown by the transition between pressure and cavitation area, where with increasing oil temperature, the transition is shifted to higher pressure levels (see detailed view). Consequently, with constant pressure but increasing temperatures, the generation of separate gas masses is favored.

It should be noted that, according to the assumptions of the two-phase model, a lubricant fraction of $F \geq 1$ can be interpreted as a compression of the oil. However, when deriving the Reynolds equation, an incompressible fluid was postulated. For achieving consistency between the Reynolds equation and two-phase model, the range of the lubricant fraction is limited to $0 \leq F \leq 1$. Thus, a fully filled gap occurs for $F = 1$. Furthermore, the time invariance of the total gas mass leads to the restriction of a theoretical maximum solvable mass. Gas masses that can penetrate from the environment via the bearing edges into the lubrication gap are not considered. In addition, the inertia for bubble growth is neglected within the model. The state of equilibrium between current and reference bubble conditions is established immediately. Also note that the Reynolds equation for incompressible fluids is evaluated even if gas is present in the lubrication gap. The lubricant fraction is used to take the influence of the gas distribution on the pressure
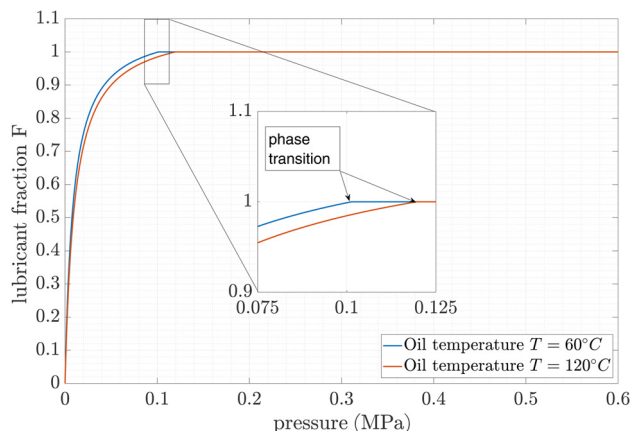

Fig. 7 Influence of oil temperature on the lubricant fraction, according to Eq. (17)

build-up into account. For this purpose, the oil properties are scaled with the lubricant fraction F, see Eq. (7).

The described relationship between lubricant fraction and hydrodynamic pressure and oil temperature, respectively, is summarized via

$$m_{B0} = m_B \tag{15}$$

$$r_B = r_{B0} \frac{p_0 T}{p T_0} - \alpha_B \frac{p T_0 - p_0 T}{p T_0} \tag{16}$$

$$F = \frac{p}{(r_{B0} + \alpha_B) p_0 \frac{T}{T_0} + (1 - \alpha_B) p} \tag{17}$$

For the numerical implementation of the two-phase model, the introduction of a pressure-related lubricant fraction

$$F_D = \frac{F}{p} = \frac{1}{(r_{B0} + \alpha_B) p_0 \frac{T}{T_0} + (1 - \alpha_B) p} \tag{18}$$

is recommended. This provides the advantage of determining the hydrodynamic pressure in both the pressure and cavitation domains. Furthermore, stabilization methods such as the first-order upwind and the Newton–Raphson method for solving the Reynolds equation can be applied.

The Reynolds equation with mass-conserving cavitation according to the two-phase model reads

$$0 = -\frac{\partial}{\partial x}\left(\frac{\rho_{\text{liq}} h^3}{12 \eta_{\text{liq}}} \frac{\partial p}{\partial x}\right) - \frac{\partial}{\partial y}\left(\frac{\rho_{\text{liq}} h^3}{12 \eta_{\text{liq}}} \frac{\partial p}{\partial y}\right)$$
$$+ \frac{\partial}{\partial x}\left(\rho_{\text{liq}} h \frac{u_S + u_H}{2} F_D p\right) + \frac{\partial}{\partial t}\left(\rho_{\text{liq}} h F_D p\right) \tag{19}$$

for journal bearings and

$$0 = -\frac{\partial}{r \partial r}\left(r \frac{\rho_{\text{liq}} h^3}{12 \eta_{\text{liq}}} \frac{\partial p}{\partial r}\right) - \frac{\partial}{r \partial \varphi}\left(\frac{\rho_{\text{liq}} h^3}{12 \eta_{\text{liq}}} \frac{\partial p}{r \partial \varphi}\right)$$
$$+ \frac{\partial}{r \partial \varphi}\left(\rho_{\text{liq}} h \frac{u_{\varphi S} + u_{\varphi H}}{2} F_D p\right) + \frac{\partial}{\partial t}\left(\rho_{\text{liq}} h F_D p\right)$$
$$+ \frac{\partial}{r \partial r}\left(\frac{\rho_{\text{liq}}^2 h^3}{\eta_{\text{liq}}}\left(\frac{u_{\varphi S}^2}{40} + \frac{u_{\varphi S} u_{\varphi H}}{30} + \frac{u_{\varphi H}^2}{40}\right) F_D p\right) \tag{20}$$

for thrust bearing, respectively.

Regarding the boundary conditions for the run-up simulations, constant pressure is assumed in the supply hole for the journal and thrust bearing. Furthermore, a distinction is made at bearing edges due to outgassing processes. If a pressure domain is present, the bearing edge pressure is equal to the atmospheric pressure. If cavitation occurs, the pressure gradient at the bearing edge is set to zero so the oil can flow off freely. For the numerical implementation of the free-draining, Fig. 8 is explained in more detail.

The pressure distribution in bearing width direction is approximated by a quadratic function

$$p(y) = a + b y + c y^2 \tag{21}$$

with the boundary conditions

$$p(y = 0) = p_1$$
$$p(y = \Delta y) = p_2 \tag{22}$$
$$p(y = 2 \Delta y) = p_3$$

where $p_{1,2,3}$ are the pressure values at the corresponding node, and Δy is the distance between them. The derivation of Eq. (21) leads to
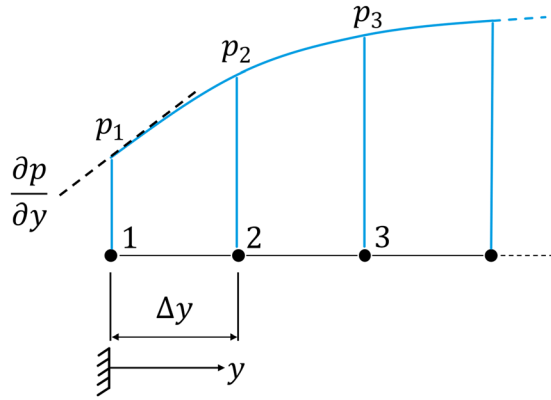
Fig. 8 Pressure gradient at bearing edge. *y* is the coordinate in bearing width direction, and Δy is the distance between the nodes due to the meshing. The bearing edge is located at node one.

$$\left.\frac{\partial p}{\partial y}\right|_{y=0} = 0 = \frac{3p_1 - 4p_2 + p_3}{2\Delta y} \tag{23}$$

After applying the finite volume method, a system of equations is obtained. Due to the a priori unknown lubricant distribution, the system of equations is solved iteratively. In each iteration step, the solution domain is subdivided again into pressure and cavitation regions. In the case of cavitation, the entries within the coefficient matrix are replaced by Eq. (23) for the considered node, and the right side is set to zero.

2.3 Temperature Model. In addition to outgassing processes, the influences of the oil temperature and the heat conduction processes at shaft, bushing, and housing must be considered for detailed modeling of the bearing properties.

To determine the lubricant film temperature in journal bearings, the 3D energy equation

$$\frac{\partial T}{\partial t} + u\frac{\partial T}{\partial x} + v\frac{\partial T}{\partial y} + w\frac{\partial T}{\partial z}$$
$$= \frac{\lambda}{\rho\,c_p}\left[\frac{\partial}{\partial x}\left(\frac{\partial T}{\partial x}\right) + \frac{\partial}{\partial y}\left(\frac{\partial T}{\partial y}\right) + \frac{\partial}{\partial z}\left(\frac{\partial T}{\partial z}\right)\right]$$
$$+ \frac{\eta}{\rho\,c_p}\left[\left(\frac{\partial u}{\partial z}\right)^2 + \left(\frac{\partial v}{\partial z}\right)^2\right] \tag{24}$$

is evaluated, where T is the oil temperature, λ, ρ, c_p are the oil properties concerning the heat conduction coefficient, density, and specific heat capacity, and (u, v, w) is the 3D velocity field of the fluid. Furthermore, a Cartesian coordinate system is used with x as circumferential, y as width, and z as gap height coordinate.

The velocity profiles and their change over the gap height are already known when deriving the Reynolds equation and can be calculated via

$$u(z) = \frac{\partial p}{\partial x}\left[I_1 - \frac{F_1}{F_0}\cdot I_0\right] + \frac{I_0}{F_0}(u_S - u_H) + u_H \tag{25}$$

$$v(z) = \frac{\partial p}{\partial y}\left[I_1 - \frac{F_1}{F_0}\cdot I_0\right] \tag{26}$$

and

$$\frac{\partial u}{\partial z} = \frac{1}{\eta}\left[\frac{\partial p}{\partial x}\left(z - \frac{F_1}{F_0}\right) + \frac{u_S - u_H}{F_0}\right] \tag{27}$$

$$\frac{\partial v}{\partial z} = \frac{1}{\eta}\frac{\partial p}{\partial y}\left(z - \frac{F_1}{F_0}\right) \tag{28}$$

with the coefficients

$$F_0 = \int_{z=0}^{h}\frac{1}{\eta}dz, \quad F_1 = \int_{z=0}^{h}\frac{z}{\eta}dz,$$
$$I_0 = \int_{z=0}^{z}\frac{1}{\eta}dz, \quad I_1 = \int_{z=0}^{z}\frac{z}{\eta}dz \tag{29}$$

For the sake of simplicity, the fluid flow w in the gap height direction is neglected in the run-up simulations. Only the flow components in circumferential u and width direction v are considered.

With the evaluation of the velocity field, the convective and dissipative parts of the energy equation are known, so subsequently, the temperature can be calculated by applying numerical methods such as the finite volume method. It is important to note that the effective lubricant properties, according to Eq. (7), should be used. Under the assumption of a fully filled gap, there would be an overestimation of dissipation and heat generation.

To determine heat conduction processes in supporting elements, the heat conduction equation

$$\frac{\partial T_{S,H}}{\partial t} = \frac{\lambda}{\rho\,c}\left[\frac{\partial}{r\partial\varphi}\left(\frac{\partial T_{S,H}}{r\partial\varphi}\right) + \frac{\partial}{r\partial r}\left(r\frac{\partial T_{S,H}}{\partial r}\right) + \frac{\partial}{\partial z}\left(\frac{\partial T_{S,H}}{\partial z}\right)\right] \tag{30}$$

is solved, where $T_{S,H}$ is the temperature of shaft and housing, respectively, and r, φ, z are equal to the coordinates in bearing circumferential, width, and radial direction.

For an efficient solution of the thermodynamics equations, the implementation is done as a fully coupled system, see Fig. 9. The lubricating films, the bushing, and housing are spatially meshed, but only the shaft has a two-dimensional meshing. A shaft meshing in radial and axial direction is sufficient because it is assumed that constant temperatures occur over the circumference due to the high rotational velocities.

With regard to the transition conditions between fluid and solid domain, pure heat conduction is assumed, since the oil adheres to the surface (conjugate heat transfer model). The implementation offers the advantage that heat transfer coefficients, which are difficult to determine, are avoided. Furthermore, a harmonic averaging
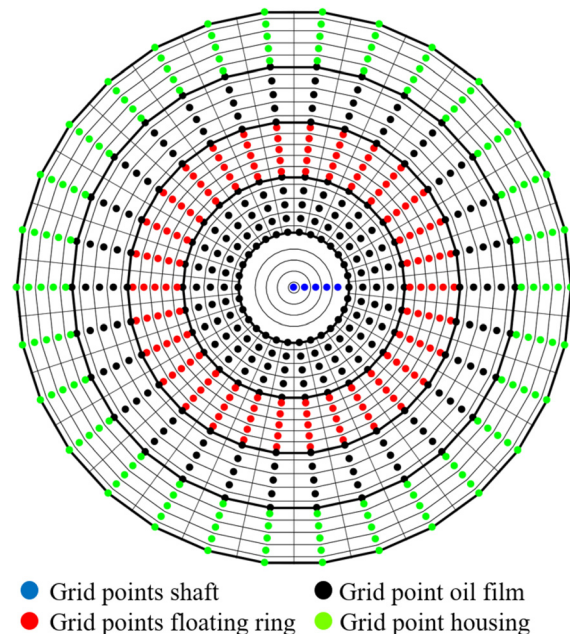

● Grid points shaft ● Grid point oil film
● Grid points floating ring ● Grid point housing

Fig. 9 Meshing of the lubrication gaps and supporting elements

technique is implemented to ensure heat flow continuity in the transition domain [57,58].

Subsequently, the thermal boundary conditions are explained in more detail, cf. Fig. 10.

First, the boundary conditions for the inner and outer oil film are discussed. For the outer lubrication gap, a constant oil temperature is set within the supply hole. Since the circumferential groove is sufficiently deep and the oil is distributed evenly over the circumference, the supply temperature is obtained in the entire groove area. Furthermore, the oil can flow from the outer to the inner gap through the connecting channels. For simplicity, a perfect mixing temperature is assumed in the groove area at the inner gap. The oil mixing temperature results from balancing the heat flow entering and leaving the groove area. Moreover, it should be noted that the oil can flow freely out of the bearing over the lateral edge. Under these circumstances, adiabatic boundary conditions are implemented at the axial boundaries of the lubricant, wherein the temperature gradient is set to zero. Finally, ideal adhesion between the solid and fluid domains is assumed, so pure heat conduction processes occur at the transition area.

Furthermore, boundary conditions for the shaft, bushing, and housing have to be defined. The yellow marked lines in Fig. 10 represent the edges of the mesh (edges of the solution domain). The red dashed lines symbolize additional locations outside the solution domain, where boundary temperatures can also be applied. This enables the consideration of temperature known from measurements or simulations. Between the red and yellow boundaries, heat conduction over the distance l_i is assumed. For the bushing, adiabatic temperature boundary conditions are assumed at the lateral edges.

Within the measurement, the temperatures were captured on the shaft (close to the journal bearing), bushing, and housing. Within the simulations, the shaft and housing temperatures are specified depending on the rotor speed. Subsequently, the bushing temperature serves for comparison.

2.4 Coupling of Hydro- and Thermodynamics. For modeling of the bearing state, the mutual interaction between hydrodynamic and thermodynamic processes is also considered, see Fig. 11.
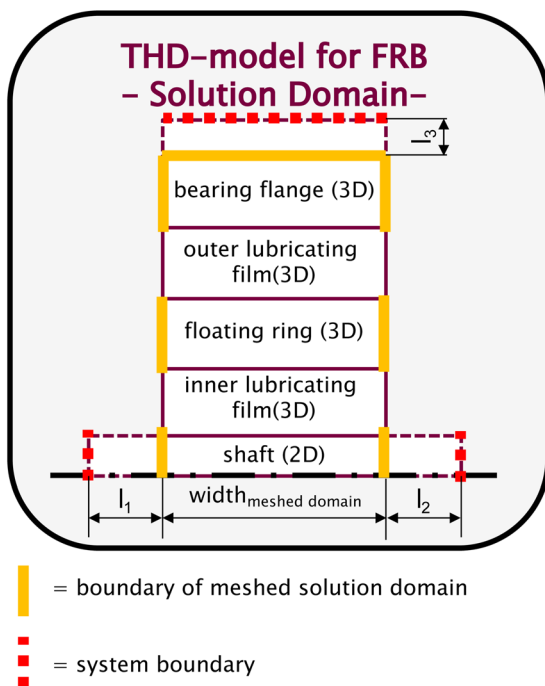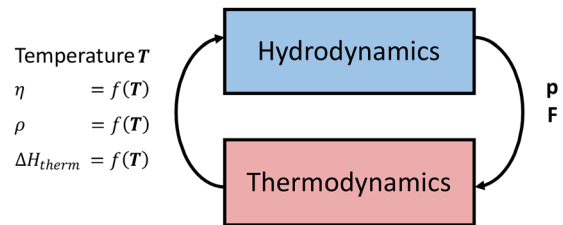

Fig. 11 Mutual influence of hydrodynamics and thermodynamics, according to Ziese et al. [26]

Starting from point of view of hydrodynamics, the Reynolds equation is solved, wherein the hydrodynamic pressure depends on the lubrication gap including thermal gap changes and the temperature-dependent oil properties. The change of viscosity is described by the Vogel equation

$$\eta(T) = a \, \exp\left(\frac{b}{T+c}\right) \tag{31}$$

where the coefficients a, b, c depend on the used oil [1]. In contrast, it is assumed that the temperature does not influence the oil density. At this point, it should be noted that with the solution of the 3D energy equation, the lubricant properties are also spatially present in the lubrication gap. When using the Reynolds equation, it is recommended to average the oil properties over the gap height. It is not recommended to average the temperature followed by determining the oil properties, because this procedure would underestimate the nonlinear dependence of the viscosity on the oil film temperature. In summary, the 3D oil properties should be calculated first and subsequently averaged over the gap height. Furthermore, it is worth to note that the oil temperature can influence the outgassing process und consequently the pressure distribution, cf. Eqs. (17) and (7). An increase of the oil temperature would shift the phase transition to higher pressure range and thus favor the occurrence of gas in the lubrication gap. An increase of gas in the gap results in a softer bearing behavior.

The thermal gap change is described via

$$\Psi(T) = \Psi_{\mathrm{ref}} + \left(\alpha_H - \alpha_S \frac{d_S}{d_H}\right)\left(T_{S/H} - T_{\mathrm{ref}}\right) \tag{32}$$

where Ψ is the relative clearance, $\alpha_{S/H}$ is the thermal expansion coefficient, and $d_{S/H}$ is the diameter of the housing and shaft [1]. With knowledge of the temperature distribution on the surface of the supporting elements, the thermal gap change can be determined, assuming a uniform change over the circumference.

With evaluation of the Reynolds equation including two-phase model, the pressure and lubricant distribution is known, so the fluid velocities and their change over the gap height can be calculated (Eqs. (25)–(28)) to determine the dissipative and conductive parts of the 3D energy equation (24).

Since the oil temperature is also influenced by the surface temperatures of the supporting elements, the 3D energy and heat conduction equation are solved as a fully coupled system (conjugate heat transfer model). With knowledge of the temperature distribution at oil, shaft, and housing, the oil properties and lubrication clearance can be updated, which are input for the hydrodynamics.

It is worth mentioning that the thermodynamic equations do not have to be solved in every step of time integration, since thermodynamic processes occur more slowly than hydrodynamic processes. Furthermore, the turbocharger is slowly accelerated during the measurements, so quasi-stationary temperature distributions can be assumed.

2.5 Validation of Hydro- and Thermodynamics. The validation of the developed hydrodynamics routines for the journal

Fig. 10 Thermal boundary conditions at floating ring bearing

and thrust bearing was already carried out in Refs. [26] and [28]. In Ref. [28], on the one hand, a journal bearing supported rigid shaft under dynamic load and, on the other hand, a full-floating ring supported Jeffcott rotor under the influence of lubricant film cavitation were investigated. With respect to the journal bearing, a comparison was made with the results of Ausas et al. [59]. This includes the shaft motion orbit, the normalized eccentricity, and the resulting bearing forces. In Ref. [26], the vibration behavior of a Jeffcott rotor [29] is investigated under the assumption of a fully filled lubrication gap (half-Sommerfeld cavitation) and the two-phase model. The evaluation includes the rotor response behavior in the frequency domain and the normalized eccentricity. Furthermore, the pressure and lubricant distribution at given rotor speed was shown. In summary, when a multiphase flow was considered, subsynchronous oscillations were observed over a larger speed range, which gives better agreement with Eling's results. Validation of the thrust bearing is documented in Ref. [26], wherein the pressure and lubricant distribution is compared with the results of Hao and Gu [60].

The validation of the thermodynamics routines is done in Ref. [61]. Therein, a journal bearing supported Jeffcott rotor was investigated at various thermal boundary conditions. The run-up simulations were performed assuming constant temperatures, lumped mass model, and evaluation of 3D energy equation.

3 Results of Run-Up Simulations

First, the run-up process is described. The rotor's motions are captured at sealing disk. Since the rotor accelerated only slowly up to the maximum speed, the assumption of quasi-stationary temperature distributions is valid. Due to the measurement of the gas flow at the compressor and turbine wheel, the axial forces can be calculated and used as input for the simulation via speed-dependent look-up tables.

Concerning the boundary conditions at the floating ring bearing, a constant pressure within the feeding holes is assumed over the entire run-up. Since there is a circumferential groove at the outer lubrication gap, the supplied oil can distribute evenly over the circumference, so there is sufficient lubricant at the outer gap. For ensuring sufficient oil at inner gap, the connecting channels of the bushing have the same angular position as the feeding holes. Consequently, a portion of the supplied lubricant can flow directly to the inner gap. Furthermore, the oil can drain freely over the bearing's edges because there is no sealing effect. Concerning the thermal boundary conditions, a constant oil inlet temperature is assumed. Furthermore, the temperatures at shaft, bushing, and housing were measured. The heating at shaft and housing is included as boundary condition for the calculations, while the bushing temperature is used for comparison between measurement and simulation.

With respect to the thrust bearing, the lubricant films can be considered separately from each other due to their arrangement and separate oil supply. Here, constant pressure at the feeding hole and atmospheric pressure at the inner and outer edges is assumed. The temperature development for the axial oil film is specified via a look-up table.

3.1 Shaft Motion in Frequency Domain. Following, the shaft motion measurement in the frequency domain is discussed, see Fig. 12. Unbalance-induced vibrations are present during the entire run-up, where the resonance occurs at $f_{\text{Rot}} = 0.24$. With further increase of the rotational frequency, the unbalance oscillations decrease, but they are still present up to the maximum speed. Subsynchronous oscillations are detected between $f_{\text{Rot}} = 0.48 - 1.0$, where at the beginning of the oil-whip, the rotor response frequency is $f = 0.16$.

Within the simulations, the rotor accelerates from the minimum to the maximum speed within 10 s, and the FE-model has 42 degrees-of-freedom overall. For the application of the finite volume method, the lubricating films and supporting elements have
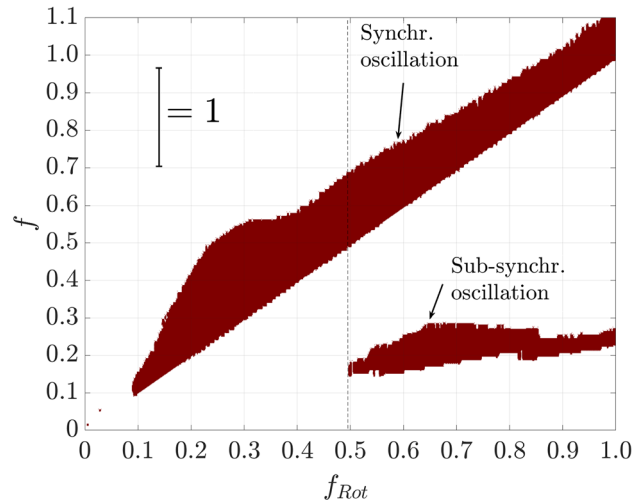

Fig. 12 Spectrogram of the shaft motion measurement captured at sealing disk

to be discretized. A mesh with 80×13 nodes (circumference × width direction) was chosen for the journal bearing. In the gap height direction, ten nodes were used for the inner and outer gap, seven nodes for the bushing, and five nodes for the housing. Due to the high rotational speed of the shaft, rotationally symmetrical elements were used. The shaft mesh is 13×10 in bearing width and shaft thickness. The lubrication gap at thrust bearing was discretized with 30×12 (circumferential and radial direction) nodes for each segment, including groove. The Reynolds equations are solved at each step of time integration within the run-up simulation, while the energy and heat conduction equations are evaluated every 5 ms. The ode23t algorithm (Runge–Kutta 2/3 order) was used as time integration method. A relative and absolute accuracy of 1.0×10^{-4} was chosen for the solver settings. Using these solver settings, the total computing time is 45 h (using multithreading[1] [62]).

The spectrograms of the run-up simulations under the assumption of half-Sommerfeld cavitation and the two-phase model are shown in Figs. 13(a) and 13(b). Neglecting outgassing processes, subsynchronous rotor oscillations can already be detected. Compared to the measurement, these occur at higher speed range from $f_{\text{Rot}} > 0.66$. The late start of the oil-whip is due to the overestimated bearing stiffness and damping since an always filled lubrication gap regardless of operating bearing condition is assumed both in floating ring and thrust bearings. The occurrence of unbalance resonance shows already a good agreement with the measurement. In comparison, better simulation results are achieved by taking outgassing processes into account, see Fig. 13(b). Here, an oil-whip is already observed at $f_{\text{Rot}} = 0.50$. With the occurrence of two-phase flow, a softer bearing behavior is obtained, so the half-whirl frequency of the journal bearing can excite a current natural frequency of the rotor. A summary of the results can be found in Table 1.

3.2 Shaft Motion in Time Domain. Besides the evaluation of the shaft motion in the frequency domain, this section deals with the prediction of the vibration amplitudes in the time domain, cf. Fig. 14. The signal is calculated over the half of difference between upper and lower envelope of the time signal and represents the rotor magnitudes around its stationary position. Consequently, the time signal contains both synchronous and subsynchronous rotor responses.

---

[1]For using multiple kernels, the runtime library of FORTRAN is set to "multithreaded," and the INTEL MATH KERNEL LIBRARY is switched to "parallel." Thus, the PARDISO solver can use multiple kernels.
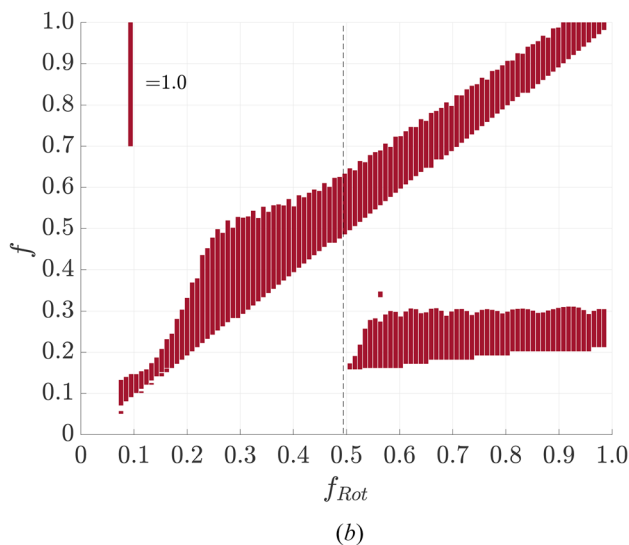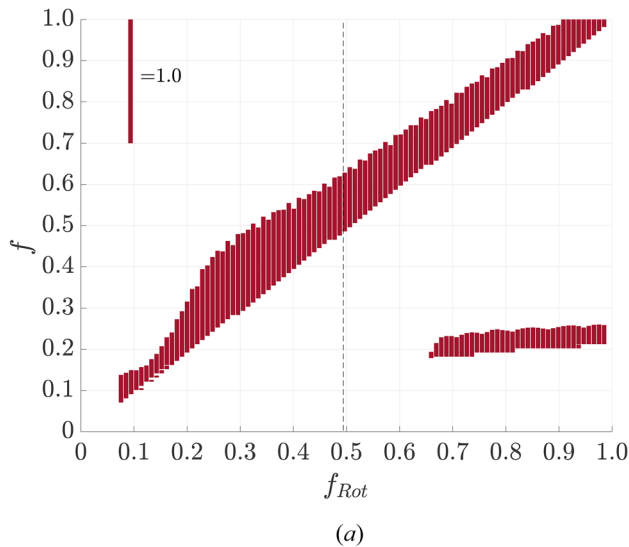
(a)

(b)

Fig. 13   Spectrogram of the shaft motion captured at sealing disk: (a) simulation with half-Sommerfeld cavitation and (b) simulation with two-phase model

Table 1   Summary of rotor response behavior

Description	Synchronous resonance	Start of oil-whip	Response frequency
Measurement	0.24	0.48	0.16
Half-Sommerfeld	0.23	0.66	0.18
Two-phase flow	0.23	0.50	0.15

Regarding the run-up measurements, subsynchronous oscillations are characterized by a stronger oscillation of the time signal and an increase of the shaft displacement ($f_{Rot} > 0.48$). With start of the oil-whip, a maximum rotor amplitude of $\hat{s}_x = 0.55$ occurs at $f_{Rot} \approx 0.65$. The run-up simulation assuming half-Sommerfeld cavitation shows a maximum displacement $\hat{s}_x = 0.39$ at $f_{Rot} \approx 0.68$. The discrepancies with the measurement result from the already mentioned overestimated stiffness and damping of the bearings. Taking outgassing processes into account, the maximum amplitudes during oil-whip are $\hat{s}_x = 0.52$ at $f_{Rot} \approx 0.51$.

3.3   Normalized Eccentricity. To investigate the influence of lubricant film cavitation on the motion of shaft and bushing more
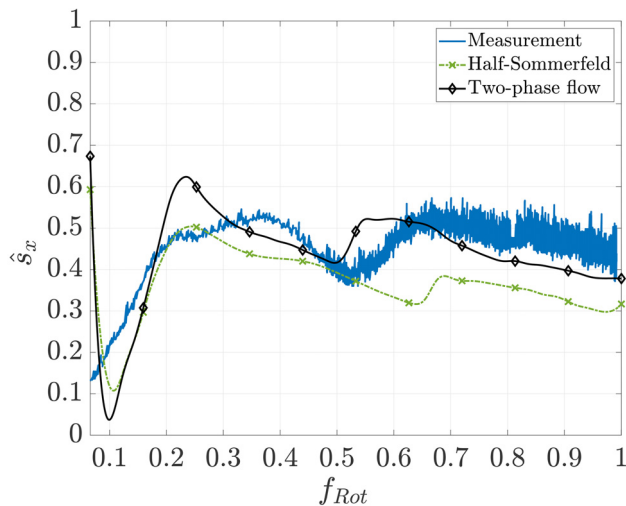

Fig. 14   Horizontal shaft motion $\hat{s}_x$ at sealing disk
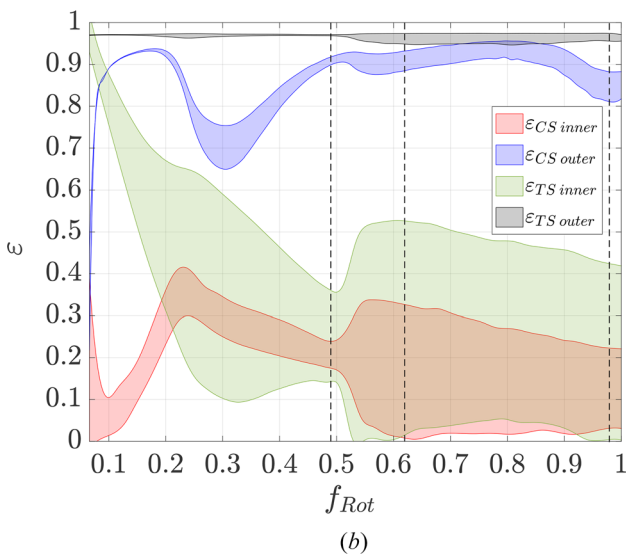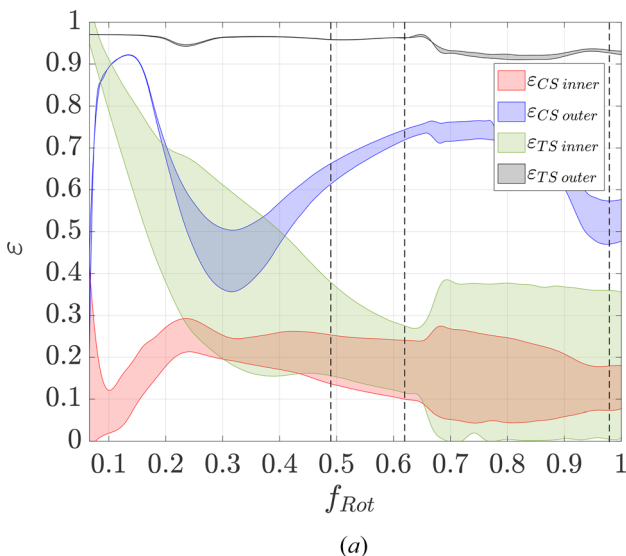

(a)

(b)

Fig. 15   Comparison of the normalized eccentricity at compressor- and turbine-sided floating ring bearing: (a) half-Sommerfeld cavitation and (b) two-phase model
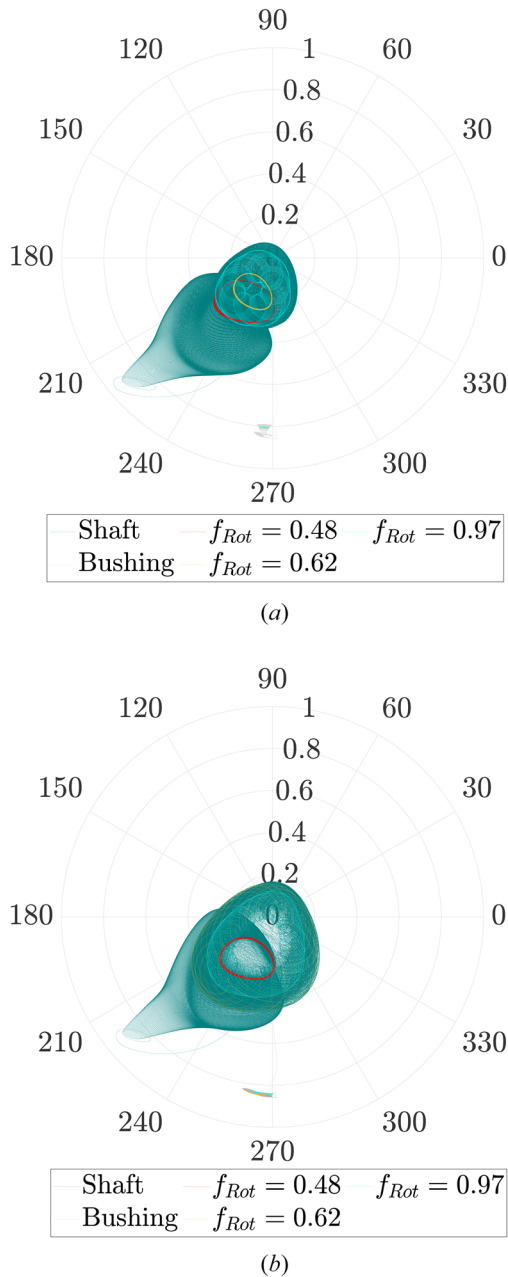
Shaft $f_{Rot} = 0.48$ $f_{Rot} = 0.97$
Bushing $f_{Rot} = 0.62$

(a)

Shaft $f_{Rot} = 0.48$ $f_{Rot} = 0.97$
Bushing $f_{Rot} = 0.62$

(b)

Fig. 16 Motion orbit at turbine-side floating ring bearing: (a) half-Sommerfeld cavitation and (b) two-phase model

in detail, the normalized eccentricity is evaluated. Based on the horizontal and vertical displacement of the supporting elements, the eccentricity is calculated via

$$\varepsilon_{inner} = \frac{1}{c_i}\sqrt{(e_{S,X} - e_{FRB,X})^2 + (e_{S,Y} - e_{FRB,Y})^2}$$
$$\varepsilon_{outer} = \frac{1}{c_a}\sqrt{e_{FRB,X}^2 + e_{FRB,Y}^2}$$

(33)

where c_i / c_a is the inner/outer bearing clearance, and $e_{S,XY} / e_{FRB,XY}$ is the horizontal and vertical displacement of shaft and floating ring, respectively. The eccentricities during the run-up are shown in Fig. 15.

First, the eccentricity of the turbine-side bushing is discussed ($\varepsilon_{TS\ outer}$). Since the rotor center of gravity is close to the turbine bearing, contact occurs at the outer lubrication gap. Assuming a fully filled lubrication gap (Fig. 15(a)), a temporary lifting of the
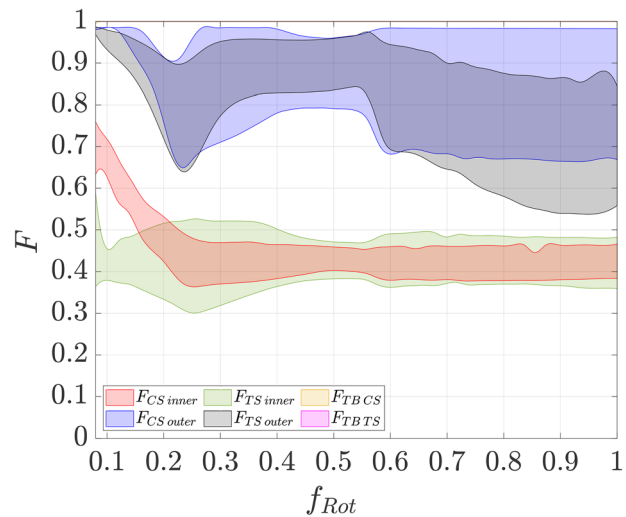

Fig. 17 Minimum lubricant fraction at thrust bearing and inner and outer gap of the floating ring bearing

bushing can be observed in case of unbalance resonance $f_{Rot} = 0.23 - 0.26$ or subsynchronous oscillation $f_{Rot} = 0.65 - 1.00$. The lifting effect can only happen if a sufficient amount of oil is squeezed, which is the case for a fully filled gap. In presence of outgassing processes (Fig. 15(b)), contact is present over the entire run-up. Thus, outgassing processes in the squeeze-film damper lead to a lower bearing damping. The effects of cavitation can also be observed on the compressor-side squeeze-film damper ($\varepsilon_{CS\ outer}$) and inner lubrication gap ($\varepsilon_{CS/TS\ inner}$) by increasing eccentricities. It should be noted that the dashed lines in Fig. 15 represent the speed range where the motion orbit is evaluated, see Fig. 16.

3.4 Motion Orbit of Shaft and Bushing. In addition to the normalized eccentricity, the motion orbit of the shaft and bushing at the turbine-side bearing is also shown for the middle speed range $f_{Rot} = 0.48$, $f_{Rot} = 0.62$ and higher rotor speed $f_{Rot} = 0.97$, see Fig. 16.

First, the bushing motion is discussed. It can be clearly seen that the bushing goes immediately into contact with the housing. A comparison between half-Sommerfeld cavitation and two-phase model shows larger bushing oscillations in presence cavitation. The motion orbit is sickle-shaped.

Subsynchronous vibrations can be observed at inner lubrication gap. Considering the rotor speed at $f_{Rot} = 0.62$ in Fig. 16(a), the oil-whip is not yet observed. The motion orbit of the shaft is determined by the rotor's unbalance condition. If the rotor speed increases further, the rotor signal is composed of the unbalance vibrations and lubricant film excitations, with the consequence of developing internal loops (see $f_{Rot} = 0.97$). Taking outgassing process into account, the inner loops of the shaft orbit can already be seen from a speed of $f_{Rot} > 0.62$.

3.5 Minimum Lubricant Fraction. The minimum lubricant fraction for the semifloating ring and thrust bearings is shown in Fig. 17. It is important to note that this is a locally varying quantity since depending on the operating bearing condition, changes occur in the lubricant distribution and thus in the local minimum.

In case of floating ring bearings, the minimum lubricant fraction is present mainly at the left and right edge, since it is a non-sealed bearing and the oil can therefore drain out freely. With regard to the inner gap of the compressor and turbine-side bearing, the lubricant fraction is between $F_{CS/TSinner} = 0.30 - 0.52$. The distribution of the lubrication fraction is influenced by the multi-lobe geometry as well as the grooves at the connecting channels. From the outer gap, it can be seen that with the occurrence of

oil-whip phenomena, the lubricant fraction varies between $F_{\mathrm{CSouter}} = 0.68 - 1.00$ at the compressor bearing and $F_{\mathrm{TSouter}} = 0.55 - 0.90$ at the turbine bearing. In contrast, both thrust bearings have a completely filled lubrication gap over the entire run-up ($F_{\mathrm{TB}} \approx 1.00$). This is due to the fact that each segment is sufficiently supplied with oil, the outer bearing edge is sealed, and the groove is deep enough so that oil is available over the entire bearing width.

3.6 Temperatures at Bushing. For further comparison of the simulation results with the measurements, the bearing temperatures are evaluated. With regard to the measurements, temperatures were captured close to the shaft surface and on the left and right side of the turbine bearing. Furthermore, temperature sensors were positioned at the bushing and bearing housing of both bearings. The temperatures at shaft and housing are used as boundary conditions for solving the energy and heat conduction equation,

whereas the heating at bushings are used for comparison. In Fig. 18, the temperature curves at the bushings during run-up are shown as temperature increase relative to the oil supply temperature.

Overall, the calculated temperatures show good agreement with the measurements. Discrepancies can be found at the compressor-side bearing, which are mainly due to the assumed temperatures at the axial boundaries of the shaft. At the compressor-side bearing, only the temperatures at the bushing and housing were measured, so the shaft temperature had to be estimated. The differences here are up to $\Delta T = 12\,^\circ\mathrm{C}$ at maximum speed (Pos.2-gray curve in Fig. 18(a)). The data situation at the turbine-side bearing was better because the shaft temperature was also measured. The temperature differences amount to a maximum of $\Delta T = 3\,^\circ\mathrm{C}$ at $f_{\mathrm{Rot}} = 0.48$ (Pos.2-gray curve in Fig. 18(b)).

3.7 Lubrication Gap at Floating Ring Bearing. In correlation with the temperature developments, heating occurs in the lubrication gap, which results in thermal gap changes. For this reason, the change of the lubrication gap over the run-up is discussed, cf. Fig. 19.

At this point, it should be mentioned that the bearing clearances were not measured directly, but calculated based on the
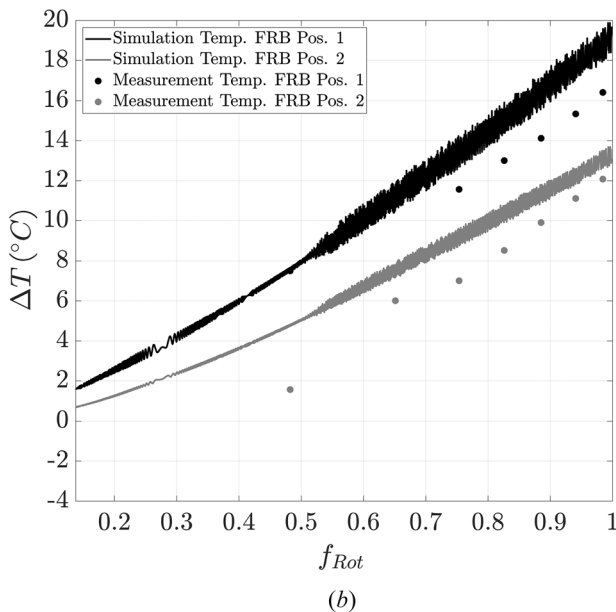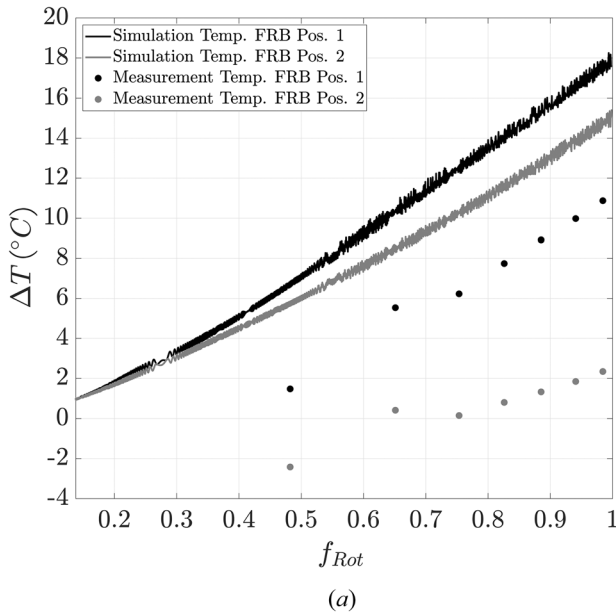

(a)

(b)

Fig. 18 Comparison of measured and calculated temperature under the assumption of two-phase flow: (a) compressor-sided and (b) turbine-sided bearing. Heating of the bushings ΔT refers to the oil inlet temperature.
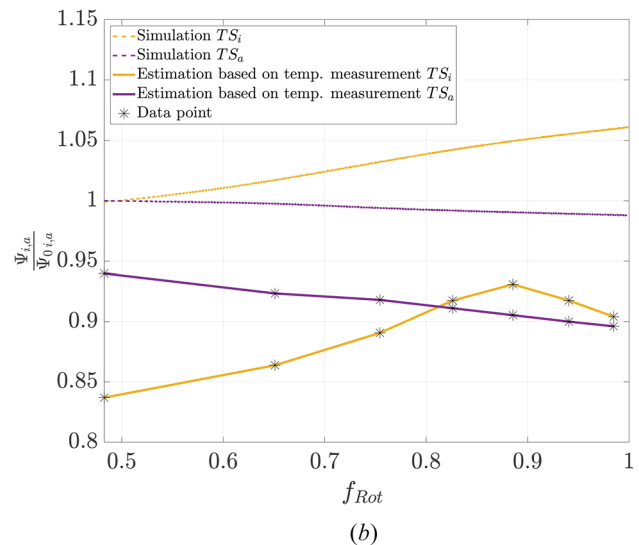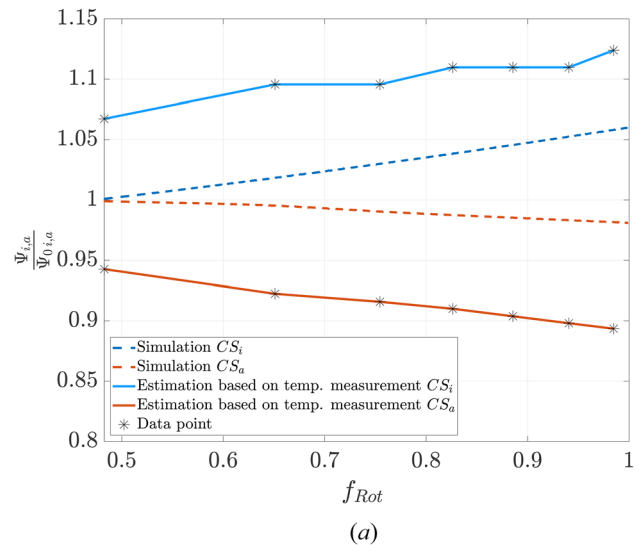

(a)

(b)

Fig. 19 Based on the temperature measurements and the solution of the heat conduction equation determined bearing clearances: (a) compressor-side and (b) turbine-side bearing. The reference clearance Ψ₀ refers to the warm bearing clearance of the corresponding gap.
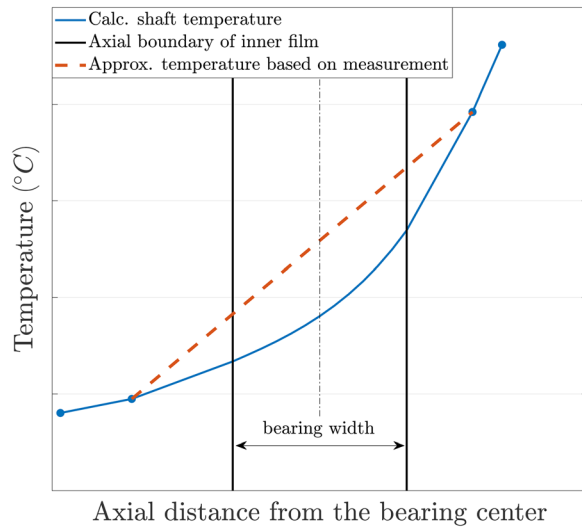
Fig. 20 Shaft temperature at turbine-sided bearing

temperatures of the supporting elements. Therefore, only a qualitative comparison can be made.

First, the outer lubrication gap is discussed, because it influences the bearing damping. The outer lubrication gap decreases both the turbine- and compressor-side bearing. This is mainly due to the increasing temperature of the bushing compared to the housing. Furthermore, the bushing has a higher thermal expansion coefficient, so that this effect is amplified. The reduction of the outer lubrication gap also means that less oil is available for squeezing. As a result, the bearing damping decreases, and thus the occurrence of subsynchronous vibrations is favored. Moreover, an increase of the inner lubrication gap can be observed during the run-up. With increasing internal gap, the bearing stiffness decreases, which also supports the occurrence of oil-whip phenomena.

An explanation for the differences in thermal gap changes is illustrated schematically in Fig. 20.

The bearing temperatures are based on an arithmetic average of the measured shaft temperatures located on the right and left side of the bearing. Subsequently, the thermal gap change is calculated via Eq. (32). The procedure provides estimated temperature at bearing center plane (dashed line), but this leads to increased errors when high temperature gradients occur, such as at turbine bearing. High temperature gradients occur at turbine bearings because, on the one hand, the hot exhaust gases are conducted into the shaft via the turbine wheel and, on the other hand, the oil has a cooling effect on the shaft. As a result of both effects, there are high temperature gradients at turbine bearing. With the solution of the energy and heat conduction equations, a more detailed representation of the thermal bearing condition is achieved (solid line), since the heat conduction processes can also be taken into account.

4 Conclusion

Within this contribution, the vibration behavior of a semifloating ring supported turbocharger rotor under the influence of lubricant film cavitation is investigated. For modeling the thermohydrodynamic behavior at journal bearing, the Reynolds equation with mass-conserving cavitation according to the two-phase model as well as the 3D energy and heat conduction equation is evaluated. Furthermore, for determining the pressure and lubricant distribution at thrust bearing, Reynolds equation with centrifugal flow and two-phase model is solved.

To illustrate the influence of cavitation, run-up simulations were carried out under the assumptions of the two-phase model or a fully filled lubrication gap (half-Sommerfeld cavitation). Assuming a fully filled lubrication gap regardless of operating bearing condition, subsynchronous vibrations can already be predicted, but these occur in a higher speed range compared to the

measurement. The reason for this is the overestimated bearing stiffness and damping at journal bearings. With the occurrence of oil-whip phenomena, stronger oscillations are observed on the rotor and bushings, so forces or hydrodynamic pressures can be generated that even lead to the lifting of the bushing. This was shown by evaluating the normalized eccentricity. The stiffness of the journal bearing is determined by the inner lubrication gap. Assuming half-Sommerfeld cavitation, sufficient oil is always transported into the narrowing gap (shear flow). Thus, the stiffness is overestimated, and lower eccentricities of the shaft can be observed. Internal loops in the motion orbit of the shaft are only observed at higher rotor speed.

The run-up simulation with consideration of mass-conserving cavitation shows better agreement with the measurements, both in the time and frequency domain. With the consideration of outgassing processes, a partially filled lubrication gap is present, which has an effect on the pressure distribution and thus on the bearing stiffness and damping. With softer bearing behavior, the start frequency of the oil-whip, the response frequency of the rotor, and its vibration amplitudes are well predicted. With regard to the normalized eccentricity at the turbine bearing, contact processes between the bushing and housing can be seen over the entire run-up. A lifting of the bushing was no longer observed. In comparison to the results with half-Sommerfeld cavitation, larger eccentricities at bushing and shaft are determined. Inner loops in the motion orbit of the shaft are already observed at middle speed range. The evaluation of the minimum lubricant fraction shows that the inner gap of the journal bearing is locally filled up to $F \approx 0.38 - 0.50$, and the outer gap is filled up to $F \approx 0.60 - 1.00$. In contrast, the gap in the thrust bearing is predominantly fully filled.

Furthermore, the temperatures at bushings were shown. Overall, a good agreement with the measurements was achieved. Discrepancies between measurements and simulations can be explained by the chosen boundary conditions and estimated shaft temperatures at compressor bearing, respectively. Based on the temperatures, the thermal gap changes were also shown. Due to the temperature developments at the bushing and housing as well as the different thermal expansion coefficients, there is a decrease of the outer gap. As a result, less oil is available for squeezing, and thus the bearing damping decreases. In contrast, the inner gap increases. The bearing's stiffness is determined by the inner lubrication gap. With increasing bearing clearance, the stiffness decreases, so that subsynchronous vibrations are favored.

Associations eV) within the framework of the industrial collective research (IGF) programme (IGF No. 18760 BR).
- FVV (Research Association for Combustion Engines eV) (FVV Project No. 1258; Funder ID: 10.13039/501100003162).

Nomenclature

a, b, c = Vogel parameter
$c_{i,a}$ = inner/outer clearance
c_p = heat capacity
d = diameter
e = eccentricity
f = ratio of the rotor response frequency and maximum speed
F = lubricant fraction
f_{Rot} = ratio of the rotor speed and maximum speed
F_D = pressure-related lubricant fraction
h = lubrication gap height
m_B = bubble mass
m_{Rot} = rotor mass
p = hydrodynamic pressure
R = specific gas constant
r_B = bubble content
r, φ, z = lubrication gap coordinates for thrust bearing
$\hat{s}_x$ = amplitude of the horizontal shaft motion
t = time
T = lubricant temperature
$u_{C,T}$ = unbalance condition at compressor/turbine wheel
$u_{S,H}$ = surface velocity of shaft/housing
u, v, w = velocity components of the lubricant flow
V = volume
x, y, z = lubrication gap coordinates for journal bearing

Greek Symbols

α_B = Bunsen coefficient
$\alpha_{S/H}$ = thermal expansion coefficient
ε = normalized eccentricity
η = viscosity of the lubricant
λ = thermal conductivity
ρ = density
Ψ = relative clearance

Indexing

$(\cdot)_B$ = bubble
$(\cdot)_{\text{CS}}$ = compressor sided
$(\cdot)_{\text{CV}}$ = control volume
$(\cdot)_{\text{dis}}$ = dissolved
$(\cdot)_{\text{eff}}$ = effective properties
$(\cdot)_{\text{FRB}}$ = floating ring bearing
$(\cdot)_g$ = gaseous phase
$(\cdot)_H$ = housing
$(\cdot)_{\text{liq}}$ = liquid
$(\cdot)_S$ = shaft
$(\cdot)_{\text{TB}}$ = thrust bearing
$(\cdot)_{\text{TS}}$ = turbine sided
$(\cdot)_{\text{undis}}$ = undissolved
$(\cdot)_{X,Y}$ = horizontal/vertical direction
$(\cdot)_0$ = reference state

References

[1] Woschke, E., Daniel, C., and Nitzschke, S., 2017, "Excitation Mechanisms of Non-Linear Rotor Systems With Floating Ring Bearings—Simulation and Validation," Int. J. Mech. Sci., **134**, pp. 15–27.

[2] Daniel, C., Woschke, E., Nitzschke, S., Göbel, S., and Strackeljan, J., 2015, "Determinismus der subharmonischen Schwingungen in gleitgelagerten Turbomaschinen," 12. Magdeburger Maschinenbau-Tage, Otto von Guericke University, Magdeburg, Germany.

[3] Koutsovasilis, P., 2019, "Automotive Turbocharger Rotordynamics: Interaction of Thrust and Radial Bearings in Shaft Motion Simulation," J. Sound Vib., **455**, pp. 413–429.

[4] Chatzisavvas, I., Boyaci, A., Lehn, A., Mahner, M., Schweizer, B., and Koutsovasilis, P., 2016, "On the Influence of Thrust Bearings on the Nonlinear Rotor Vibrations of Turbochargers," ASME Paper No. GT2016-58168.

[5] Andres, L. S., Rivadeneira, J. C., Gjika, K., Groves, C., and LaRue, G., 2007, "Rotordynamics of Small Turbochargers Supported on Floating Ring Bearings—Highlights in Bearing Analysis and Experimental Validation," ASME J. Tribol., **129**(2), pp. 391–397.

[6] Andres, L. S., and Diaz, S. E., 2003, "Flow Visualization and Forces From a Squeeze Film Damper Operating With Natural Air Entrainment," ASME J. Tribol., **125**(2), pp. 325–333.

[7] Etsion, I., and Ludwig, L., 1982, "Observation of Pressure Variation in the Cavitation Region of Submerged Journal Bearings," ASME J. Lubr. Technol., **104**(2), pp. 157–163.

[8] Jung, S., and Vance, J., 1993, "Effects of Vapor Cavitation and Fluid Inertia on the Force Coefficients of a Squeeze Film Damper Part II—Experimental Comparisons," Tribol. Trans., **36**(4), pp. 700–706.

[9] Andres, L. S., Lu, X., and Liu, Q., 2016, "Measurements of Flow Rate and Force Coefficients in a Short-Length Annular Seal Supplied With a Liquid/Gas Mixture (Stationary Journal)," Tribol. Trans., **59**(4), pp. 758–767.

[10] Andres, L. S., and Lu, X., 2018, "Leakage, Drag Power, and Rotordynamic Force Coefficients of an Air in Oil (Wet) Annular Seal," ASME J. Eng. Gas Turbines Power, **140**(1), p. 012505.

[11] Xing, C., Braun, M. J., and Li, H., 2009, "A Three-Dimensional Navier-Stokes-Based Numerical Model for Squeeze-Film Dampers. Part 1—Effects of Gaseous Cavitation on Pressure Distribution and Damping Coefficients Without Consideration of Inertia," Tribol. Trans., **52**(5), pp. 680–694.

[12] Zhang, J., and Meng, Y., 2012, "Direct Observation of Cavitation Phenomenon and Hydrodynamic Lubrication Analysis of Textured Surfaces," Tribol. Lett., **46**(2), pp. 147–158.

[13] Song, Y., Ren, X., Gu, C., and Li, X.-S., 2015, "Experimental and Numerical Studies of Cavitation Effects in a Tapered Land Thrust Bearing," ASME J. Tribol., **137**(1), p. 011701.

[14] Bai, L., Meng, Y., and Zhang, V., 2016, "Experimental Study on Transient Behavior of Cavitation Phenomenon in Textured Thrust Bearings," Tribol. Lett., **63**(2), p. 27.

[15] Kumar, A., and Booker, J. F., 1991, "A Finite Element Cavitation Algorithm," ASME J. Tribol., **113**(2), pp. 276–284.

[16] Nitzschke, S., Woschke, E., Schmicker, D., and Strackeljan, J., 2016, "Regularised Cavitation Algorithm for Use in Transient Rotordynamic Analysis," Int. J. Mech. Sci., **113**, pp. 175–183.

[17] Nowald, G., 2018, "Numerical Investigation of Rotors in Floating Ring Bearings Using Co-Simulation," Ph.D. thesis, Technical University Darmstadt, Darmstadt, Germany.

[18] Nitzschke, S., 2017, "Instationäres Verhalten schwimmbuchsengelagerter Rotoren unter Berücksichtigung masseerhaltender Kavitation," Ph.D. thesis, Otto von Guericke University, Magdeburg, Germany.

[19] Song, Y., and Gu, C., 2015, "Development and Validation of a Three-Dimensional Computational Fluid Dynamics Analysis for Journal Bearings Considering Cavitation and Conjugate Heat Transfer," ASME J. Eng. Gas Turbines Power, **137**(12), p. 122502.

[20] Franc, J., and Michel, J., 2005, Fundamentals of Cavitation (Fluid Mechanics and Its Applications), Springer, Dordrecht, The Netherlands.

[21] Brennen, E., 1995, Cavitation and Bubble Dynamics, Oxford University Press, New York.

[22] Geike, T., and Popov, V., 2009, "Cavitation Within the Framework of Reduced Description of Mixed Lubrication," Tribol. Int., **42**(1), pp. 93–98.

[23] Gehannin, J., Arghir, M., and Bonneau, O., 2009, "Evaluation of Rayleigh-Plesset Equation Based Cavitation Models for Squeeze Film Dampers," ASME J. Tribol., **131**(2), p. 024501.

[24] Nguyen-Schäfer, H., 2013, Aero and Vibroacoustics of Automotive Turbochargers, Springer, Berlin.

[25] Nguyen-Schäfer, H., 2015, Rotordynamics of Automotive Turbochargers, Springer International Publishing, Berlin.

[26] Ziese, C., Irmscher, C., Nitzschke, S., Daniel, C., and Woschke, E., 2021, "Run-Up Simulation of a Semi-Floating Ring Supported Turbocharger Rotor Considering Thrust Bearing and Mass-Conserving Cavitation," Lubricants, **9**(4), p. 44.

[27] Fuchs, A., Klimpel, T., Dan, K. H., and Rohne, J. S., 2017, "Comparison of Measured and Calculated Vibrations of a Turbocharger," SIRM, Graz, Austria, pp. 1–10

[28] Ziese, C., Nitzschke, S., and Woschke, E., 2021, "Run Up Simulation of a Full-Floating Ring Supported Jeffcott-Rotor Considering Two-Phase Flow Cavitation," Arch. Appl. Mech., **91**(2), pp. 777–790.

[29] Eling, R., 2018, "Towards Robust Design Optimization of Automotive Turbocharger Rotor-Bearing Systems," Ph.D. thesis, Delft University of Technology, Delft, The Netherlands.

[30] Nowald, G., Scholl, R., and Schweizer, B., 2017, "Influence of Fluid Film Cavitation Effects on the Stability of Rotors in Journal Bearins," VIRM, Vol. 11, Manchester, UK, Mar. 10.

[31] Boyaci, A., and Schweizer, B., 2015, "Nonlinear Oscillations of High-Speed Rotor Systems in Semi-Floating Ring Bearing," Ninth IFToMM International Conference on Rotordynamics, Mechanisms and Machine Science 21, Milan, May 26, pp. 845–854.

[32] Liang, F., Zhou, M., and Xu, Q., 2016, "Effects of Semi-Floating Ring Bearing Out Clearance on the Subsynchronous Oscillation of Turbocharger Rotor," Chin. J. Mech. Eng., **29**(5), pp. 901–910.

[33] Gjika, K., Andrés, L. S., and Larue, G. D., 2010, "Nonlinear Dynamic Behavior of Turbocharger Rotor-Bearing Systems With Hydrodynamic Oil Film and Squeeze Film Damper in Series: Prediction and Experiment," ASME J. Comput. Nonlinear Dyn., 5(4), p. 041006.

[34] Schweizer, B., 2010, "Dynamics and Stability of Turbocharger Rotors," Arch. Appl. Mech., 80(9), pp. 1017–1043.

[35] Woschke, E., Göbel, S., Nitzschke, S., Daniel, C., and Strackeljan, J., 2015, "Influence of Bearing Geometry of Automotive Turbochargers on the Nonlinear Vibrations During Run-Up," Proceedings of the Ninth IFToMM International Conference on Rotor Dynamics, Mechanisms and Machine Science 21, Milan, pp. 835–844.

[36] Cao, J., Dousti, S., Allaire, P., and Dimond, T., 2017, "Nonlinear-Transient Modeling and Design of Turbocharger Rotor/Semi-Floating Bush Bearing System," Lubricants, 5(2), p. 16.

[37] Perge, J., Stadermann, M., Pischinger, S., Höpke, B., Lückmann, D., Back, A., and Uhlmann, T., 2017, "Influence of Non-Linear Rotor Dynamics on the Bearing Friction of Automotive Turbochargers," Lubricants, 5(3), p. 29.

[38] Dyk, S., Smolik, L., and Rendl, J., 2020, "Predictive Capability of Various Linearization Approaches for Floating-Ring Bearings in Nonlinear Dynamics of Turbochargers," Mech. Mach. Theory, 149, p. 103843.

[39] Chasalevris, A., 2016, "An Investigation on the Dynamics of High-Speed Systems Using Nonlinear Analytical Floating Ring Bearing Models," Int. J. Rotating Mach., 2016, p. 7817134.

[40] Nowald, G., Boyaci, A., Schmoll, R., Koutsovasilis, P., Driot, N., and Schweizer, B., 2015, "Influence of Axial Grooves in Full-Floating Ring Bearings on the Nonlinear Oscillations of Turbocharger Rotors," SIRM 2015—11th International Conference on Vibrations in Rotating Machines, Magdeburg, Germany, Feb. 23–25, p. 57.

[41] Peixoto, T., Nordmann, R., and Cavalca, K., 2021, "Dynamic Analysis of Turbochargers With Thermo-Hydrodynamic Lubrication Bearings," J. Sound Vib., 505, p. 116140.

[42] Liang, F., Xu, Q., and Zhou, M., 2015, "Predicting the Frequency of the Rotor Whirl Excited by Semi-Floating Ring Bearing," ASME Paper No. DETC2015-47062.

[43] Liang, F., Li, Y., Zhou, M., Xu, Q., and Du, F., 2017, "Integrated Three-Dimensional Thermohydrodynamic Analysis of Turbocharger Rotor and Semi-Floating Ring Bearings," ASME J. Eng. Gas Turbines Power, 139(8), p. 082501.

[44] Dong, H., Nowald, G., Lu, D., and Schweizer, B., 2019, "Numerical Analysis of Fluid-Film-Cavitation on Rotordynamic Vibration and Stability Behavior," PAMM, 19(1), p. e201900107.

[45] Boyaci, A., Lu, D., and Schweizer, B., 2015, "Stability and Bifurcation Phenomena of Laval/Jeffcott Rotors in Semi-Floating Ring Bearings," Nonlinear Dyn., 79(2), pp. 1535–1561.

[46] Boyaci, A., 2016, "Numerical Continuation Applied to Nonlinear Rotor Dynamics," Procedia IUTAM, 19, pp. 255–265.

[47] Boyaci, A., 2019, "Zum Stabilitäts- und Bifurkationsverhalten hochtouriger Rotoren in Gleitlagern," Ph.D. thesis, Karlsruher Institute of Technology, Karlsruhe, Germany.

[48] Becker, K., 2019, "Dynamisches Verhalten hydrodynamisch gelagerter Rotoren unter Berücksichtigung veränderlicher Lagergeometrien," Ph.D. thesis, Karlsruher Instiute of Technology, Karlsruhe, Germany.

[49] Gautam, S., Quamar, S., and Ghosh, M. K., 2011, "Thermal Analysis of Externally Pressurised Step Bearing Including Centrifugal Inertia Effect for a Bubbly Lubricant," Int. J. Eng., Sci. Technol., 2(11), pp. 147–166.

[50] Pinkus, O., and Lund, J., 1981, "Centrifugal Effects in Thrust Bearings and Seals Under Laminar Conditions," ASME J. Lubr. Technol., 103(1), pp. 126–136.

[51] Drapatow, T., Alber, O., and Woschke, E., 2021, "Consideration of Fluid Inertia and Cavitation for Transient Simulation of Squeeze Film Damped Rotor Systems," The 14th International Conference on Dynamics of Rotating Machinery: Proceedings of SIRM, Gdansk, Poland, p. 39.

[52] Reinhardt, E., and Lund, J., 1975, "The Influence of Fluid Inertia on the Dynamic Properties of Journal Bearings," ASME J. Lubr. Technol., 97(2), pp. 159–165.

[53] White, F., 2005, Fluid Mechanics, McGraw-Hill, New York.

[54] Dowson, D., and Taylor, C. M., 1979, "Cavitation in Bearings," Annu. Rev. Fluid Mech., 11(1), pp. 35–65.

[55] Fuchs, A., 2002, "Schnelllaufende Radialgleitlagerungen im instationären Betrieb," Ph.D. thesis, Technical University Carolo Wilhelmina zu Braunschweig, Braunschweig, Germany.

[56] Mermertas, U., 2017, "Nichtlinearer Einfluss von Radialgleitlagern auf die Dynamik schnelllaufender Rotoren," Ph.D. thesis, Technical University Clausthal, Clausthal-Zellerfeld, Germany.

[57] Paranjpe, R., and Han, T., 1994, "A Study of the Thermohydrodynamic Performance of Steadily Loaded Journal Bearings," Tribol. Trans., 37(4), pp. 679–690.

[58] Patankar, S., 1980, Numerical Heat Transfer and Fluid Flow, CRC Press, Singapore.

[59] Ausas, R. F., Jai, M., and Buscaglia, G. C., 2009, "A Mass-Conserving Algorithm for Dynamical Lubrication Problems With Cavitation," ASME J. Tribol., 131(3), p. 031702.

[60] Hao, Z. R., and Gu, C. W., 2014, "Numerical Modeling for Gaseous Cavitation of Oil Film and Non-Equilibrium Dissolution Effects in Thrust Bearings," Tribol. Int., 78, pp. 14–26.

[61] Irmscher, C., Nitzschke, S., and Woschke, E., 2019, "Transient Thermo-Hydrodynamic Analysis of a Laval Rotor Supported by Journal Bearings With Respect to Calculation Times," SIRM 2019—13th International Conference on Dynamics of Rotating Machines, Copenhagen, Denmark, Feb. 13–15, pp. 162–173.

[62] Intel, 2020, "Parallel Sparse Direct and Multi-Recursive Iterative Linear Solvers PARDISO, User Guide Version 7.2," Intel, Santa Clara, CA.